Available online at www.sciencedirect.com
ScienceDirect
Trans. Nonferrous Met. Soc. China 32(2022) 513−523
Transactions of Nonferrous Metals Society of China
www.tnmsc.cn

Effect of microvoids on microplasticity behavior of dual-phase titanium alloy under high cyclic loading (I): Crystal plasticity analysis

Kai-di LI[1], Xiao-ning HAN[2], Bin TANG[1], Meng-qi ZHANG[1], Jin-shan LI[1]

1. State Key Laboratory of Solidification Processing, Northwestern Polytechnical University, Xi'an 710072, China;
2. Beijing Aeronautical Manufacturing Technology Research Institute, Beijing 100024, China

Received 8 February 2021; accepted 20 October 2021

Abstract: A crystal plasticity finite element (CPFE) model was established and 2D simulations were carried out to study the relationship between microvoids and the microplasticity deformation behavior of the dual-phase titanium alloy under high cyclic loading. Results show that geometrically necessary dislocations (GND) tend to accumulate around the microvoids, leading to an increment of average GND density. The influence of curvature in the tip plastic zone (TPZ) on GND density is greater than that of the size of the microvoid. As the curvature in TPZ and the size of the microvoid increase, the cumulative shear strain (CSS) in the primary α, secondary α, and β phases increases. Shear deformation in the prismatic slip system is dominant in the primary α phase. As the distance between the microvoids increases, the interactive influence of the microvoids on the cumulative shear strain decreases.

Key words: crystal plasticity; dual-phase Ti alloy; microvoids; high cyclic loading; cumulative shear strain; geometrically necessary dislocation

1 Introduction

Titanium alloys are widely used in the aerospace and automotive industries, biomedical components, marine applications, and petro-chemical engineering because of the excellent properties such as high specific strength, high specific stiffness, corrosion resistance, and high temperature resistance [1−3]. Among them, the dual-phase titanium alloys are widely used owing to the great properties of the combination between hexagonal close-packed α phase and body-centered cubic β phase, such as Ti−6Al−4V alloy [4,5].

High cycle fatigue (HCF) performance is of great importance for the application of titanium alloys in aircraft engines and airframes which are often subjected to cyclic loading associated with high-frequency vibration [6,7]. The researchers concluded that the HCF performance of materials is greatly sensitive to defects (e.g., microvoids), and the fatigue strength will be greatly reduced especially when the defects distribute around the free surface [8,9]. Defects at critical stress locations will reduce the fatigue life, even if the applied stress does not increase significantly [10]. FOMIN et al [11,12] investigated the effect of subsurface porosity on fatigue cracking under cyclic loading, and conclusions showed that the fatigue limit of the fusion zone in the presence of microvoids is about 30% lower than that of the unnotched base material. VANSICKLE et al [13] found that in many cases, the cracks will propagate toward the microvoids, causing the material to fracture prematurely under cyclic loading. From the works about Mode II crack growth [14,15], microvoids could be caused by the

Corresponding author: Bin TANG, Tel: +86-13991965416, E-mail: toby@nwpu.edu.cn
DOI: 10.1016/S1003-6326(22)65812-6

distortion of the lattice, which leads to the fatigue crack to propagate on the primary slip plane. So far, there have not been many reports about the effects of microvoids in titanium alloys on the HCF performance, especially for the analysis from the microplasticity in mesoscale.

In recent years, crystal plasticity finite element method (CPFEM) has become a popular method to analyze the mechanical response of the microstructure of materials because of the abilities to effectively solve the complex boundary condition and provide great flexibility with respect to various constitutive formulations [16,17]. CPFE is also widely used to study the fatigue performance of materials [18−20]. Recently, many CPFE models have been developed to analyze the slip system interactions [21] and crack nucleation under cyclic loading [22,23]. Based on the crystal plasticity theory, MORRISSEY et al [24] found that the cumulative plastic strain in the Ti−6Al−4V alloy shows a great sensitivity to the stress ratio under high cyclic loading, and the deformation behavior is closely related to the grain orientation and phase morphology. And their work is of great significance to understand the deformation mechanism of the dual-phase titanium alloys under cyclic loading and predict the HCF life. However, there is little research on the microplasticity deformation behavior of microvoids in dual-phase titanium alloys on HCF performance based on CPFE simulation.

In this work, the HCF behavior of duplex Ti−6Al−4V alloy was studied and a 2D CPFE model was established. Different shapes, sizes and aggregated degrees of microvoids were set into the model to discuss the effects of microvoids on the microplasticity deformation behavior of the Ti−6Al−4V alloys. The hardening effect caused by geometrically necessary dislocations (GND) and cyclic softening effect were incorporated into the CPFE model. The changes of GND and cumulative shear strain (CSS) of the dual-phase titanium alloy with microvoids under high cyclic loading were discussed based on the present model.

2 Model implementation

2.1 Crystal plasticity constitutive model

The deformation of metallic material at room temperature is caused by the dislocation glide on the slip plane. The total deformation can be decomposed into elastic and plastic parts as

$$\begin{cases} \boldsymbol{F}=\boldsymbol{F}^{\mathrm{e}}\boldsymbol{F}^{\mathrm{p}} \\ \dot{\boldsymbol{F}}^{\mathrm{p}}=\boldsymbol{L}^{\mathrm{p}}\boldsymbol{F}^{\mathrm{p}} \\ \boldsymbol{L}^{\mathrm{p}}=\sum_{\alpha=1}^{N}\dot{\gamma}^{\alpha}\boldsymbol{s}^{\alpha}\otimes\boldsymbol{n}^{\mathrm{p}} \end{cases} \tag{1}$$

where $\boldsymbol{F}^{\mathrm{e}}$ is the elastic deformation gradient caused by the stretch of lattice and crystal rigid rotation. $\boldsymbol{F}^{\mathrm{p}}$ is the plastic deformation gradient corresponding to the displacement of the dislocation along the slip system. $\dot{\boldsymbol{F}}^{\mathrm{p}}$ is the time derivative of the deformation gradient. The plastic part of the velocity gradient $\boldsymbol{L}^{\mathrm{p}}$ consists of contributions from each active slip system, with normal vector $\boldsymbol{n}^{\alpha}$ and slip direction vector $\boldsymbol{s}^{\alpha}$ corresponding to the α-th slip system. $\dot{\gamma}^{\alpha}$ is the shear strain rate on the α-th slip system and N is the number of the active slip systems.

A phenomenological rate-dependent crystal plasticity constitutive model was proposed by HUTCHINSON et al [25]. The back stress $\tau_{\mathrm{b}}^{\alpha}$ is introduced into the model to describe the cyclic softening effect and has been decomposed into two parts $\tau_{\mathrm{b}_1}^{\alpha}$ and $\tau_{\mathrm{b}_2}^{\alpha}$ and both subject to the Armstrong-Frederick nonlinear kinematic hardening law [26,27]:

$$\dot{\gamma}^{\alpha}=\dot{\gamma}_0\left|\frac{\tau^{\alpha}-\tau_{\mathrm{b}}^{\alpha}}{\zeta^{\alpha}}\right|^{n}\mathrm{sgn}\left(\tau^{\alpha}-\tau_{\mathrm{b}}^{\alpha}\right) \tag{2}$$

$$\tau_{\mathrm{b}}^{\alpha}=\tau_{\mathrm{b1}}^{\alpha}+\tau_{\mathrm{b2}}^{\alpha} \tag{3}$$

$$\dot{\tau}_{\mathrm{b}_1}^{\alpha}=K_1\left(\frac{2}{3}d_1\dot{\gamma}^{\alpha}-\tau_{\mathrm{b}_1}^{\alpha}\left|\dot{\gamma}^{\alpha}\right|\right) \tag{4}$$

$$\dot{\tau}_{\mathrm{b}_2}^{\alpha}=K_2\left(\frac{2}{3}d_2\dot{\gamma}^{\alpha}-\tau_{\mathrm{b}_2}^{\alpha}\left|\dot{\gamma}^{\alpha}\right|\right) \tag{5}$$

where τ^{α}, $\dot{\gamma}_0$ and ζ^{α} are the resolved shear stress, reference shear strain rate and slip resistance of the α-th slip system, respectively, K_1, K_2 and d_2 are all material constants, and d_1 is a variable used to describe the cyclic softening behavior.

Hardening effect consists of hardening caused by statistically stored dislocations and GND. The evolution of slip resistance is determined by the following formula [28]:

$$\dot{\zeta}^{\alpha}=\sum_{\beta}h_{\alpha\beta}\left|\dot{\gamma}^{\beta}\right|+\frac{k_0\hat{\alpha}^2G^2b}{2\left(\zeta^{\alpha}-\zeta_0^{\alpha}\right)}\sum_{\beta}\lambda^{\beta}\dot{\gamma}^{\beta} \tag{6}$$

The first term in Eq. (6) is the hardening caused by the interaction between slip systems, including self-hardening and latent hardening. The slip self-hardening modulus $h_{\alpha\alpha}$ is calculated by the following formula [29,30]:

$$h_{\alpha\alpha}=h(\gamma)=h_0\mathrm{sech}^2\left|\frac{h_0\gamma}{\zeta_s-\zeta_0}\right| \tag{7}$$

where h_0 is the initial hardening modulus, ζ_s and ζ_0 are the initial slip resistance on slip system α and the saturation intensity of the slip system, respectively, and γ is the CSS in all slip systems calculated by the formula:

$$\gamma=\sum_{\alpha}\int_0^t\left|\dot{\gamma}^\alpha\right|\mathrm{d}t \tag{8}$$

The latent hardening modulus can be described as

$$h_{\alpha\beta}=qh(\gamma) \tag{9}$$

where q is the latent hardening coefficient.

Hardening caused by the GND is given by the latter term of Eq. (6), in which k_0 is a material constant, b is the magnitude of the Burgers vector, G is the shear modulus, and $\hat{\alpha}$ is a dimensionless parameter with a value of 1/3 [31−34]. Estimation of GND along the slip plane is named λ^β, expressed as

$$\lambda^\beta=\sqrt{\boldsymbol{\Lambda n}^\beta:\boldsymbol{\Lambda n}^\beta} \tag{10}$$

where $\boldsymbol{n}^\beta$ is the normal direction of slip plane, and the Nye tensor [35] expressing GND can be obtained by calculating the deformation incompatibility $(\boldsymbol{F}^{\mathrm{e}})^{-1}$ such as

$$\Lambda=-\nabla\times(\boldsymbol{F}^{\mathrm{e}})^{-1} \tag{11}$$

2.2 Material parameters and model design

The parameters of the crystal plasticity constitutive model are obtained. The stiffness matrix components of the α phase are C_{11}=162400 MPa, C_{12}=92000 MPa, C_{13}=69000 MPa, C_{33}=180700 MPa and C_{44}=49700 MPa [36]. Parameters of three families of slip systems are listed in Table 1. Only 12 $\langle 110\rangle\{1\bar{1}1\}$ slip systems of the β phase are considered in this model, as shown in Table 2. The elastic modulus and Poisson's ratio of β phase are set to 85000 MPa and 0.35, respectively. The crystal plasticity constitutive model has been coded into ABAQUS/Standard through the user material subroutine (UMAT).

The stress concentration mainly appears at the tip of the microvoid, e.g., tip plastic zone (TPZ) (Fig. 1(a)). An equivalent model is designed (Fig. 1(b)). Some works studied the effects of the size of a circular microvoid on the deformation of materials by changing the diameter of the

Table 1 Crystal plasticity model parameters

Slip system	$\dot{\gamma}_0$/s^{-1}	n	h_0/MPa	ζ_s/MPa	ζ_0/MPa
Basal $\langle a\rangle$			631.2	462	420
Prismatic $\langle a\rangle$	0.001	15	436.2	407	370
Pyramidal $\langle a\rangle$			436.2	539	490

Table 2 Crystal plasticity constitutive parameters of β phase

Slip system	$\dot{\gamma}_0$/s^{-1}	n	k_0	h_0/MPa	ζ_s/MPa	ζ_0/MPa
$\langle 110\rangle\{1\bar{1}1\}$	0.001	15	2	100	333	366

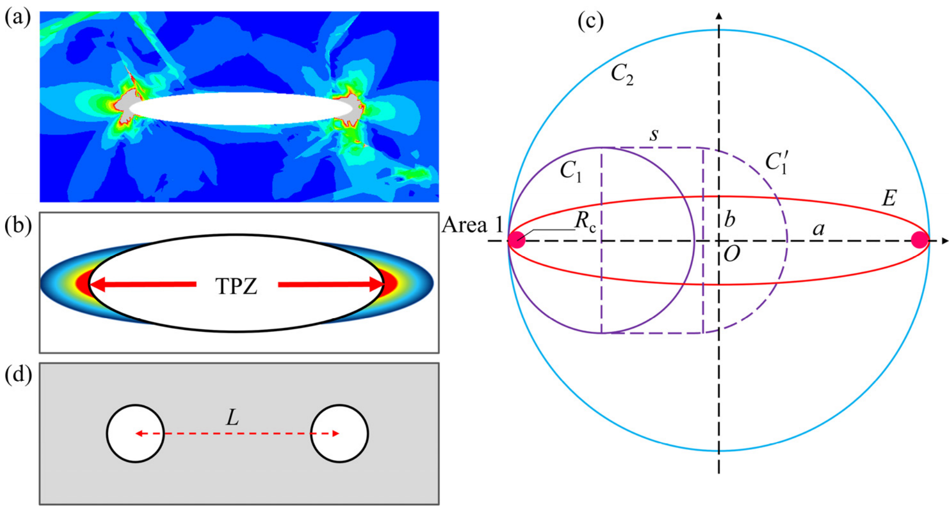

Fig. 1 Model design: (a) Distribution map of stress in defective model; (b) Equivalent model of stress distribution around void; (c) Geometrical diagram of description of void parameters; (d) Diagram of double-voids model

microvoid [37]. The geometric characteristics of circular microvoid can be decomposed into two parts: size and shape. As shown in Fig. 1(c), when increasing the diameter of circle C_1 to circle C_2, the curvature in Area 1 becomes smaller at the same time. Therefore, to study the effect of the size of the microvoid on the HCF behavior of the materials, it is better to adjust the magnitude of s to change the size of the microvoid and keep the curvature in Area 1 constant, such as circle C_1' in Fig. 1(c). And the microvoid size $S_v=\pi ab$ should be kept constant during the process of changing the microvoid curvature $k=R_c^{-1}$. The coupled effect of multi-voids can be studied by introducing multi-voids with different distances L between them (Fig. 1(d)) with the constant size of the void and TPZ curvature.

2.3 Finite element implementation

In order to generate the duplex microstructure of Ti−6Al−4V alloy, a script of the slice segmentation method was written in Python. The process is divided into four parts: firstly, generate the Voronoi model with no lamellar template; secondly, generate several lamellar templates with different spatial orientations; then, perform Boolean operations on individual grains and lamellar templates to obtain lamellar clusters; at last, the remaining equiaxed crystals and the lamellar clusters just generated are spliced to realize the duplex microstructure model. The 2-dimensional 8-node element CPS8 was used to mesh the model.

In this work, a microstructure model of Ti−6Al−4V alloy containing 25 grains or 100 grains with a primary α phase content of 40% was established (Fig. 2). Because the GND density is calculated by the average GND density of the microstructure in this work, the model using 100 grains is used for simulation. The average GND density of grains in the white dotted frame of the 100-grain model in Fig. 2(b) is counted to weaken the boundary effects. Different from the analysis of GND, the study of CSS only considers the changes of CSS in the local area around the void. The 25-grain model is used for improving the calculation efficiency (Fig. 2(a)). Voids with curvatures k from 0.0032 to 15.7216 μm^{-1} or sizes S_v from 19.63 to 89.63 μm^2 or different degrees of aggregation are introduced into the model to study the interactive effects of the voids on the cumulative shear strain of each phase or each slip system. The grains with an average grain size of 12 μm in the model are randomly oriented, and the thickness of lamellar α phase and lamellar β phase is set to be 2 and 0.5 μm, respectively. The applied stress is along the y direction in Fig. 2, and the loading form is a sine wave by the following formula:

$$\sigma=\sigma_{max}\sin(125\pi t) \tag{12}$$

where σ is the applied stress, σ_{max} is the nominal maximum stress at 350 MPa, and t is the loading time. A total of 100 cycles of fatigue loading were performed in this work, and the loading frequency was 125 Hz. Edges 1-3 and 3-4 are respectively constrained in the x and y directions, and Edge 1-2 is subjected to cyclic loading along the y direction (Fig. 2(a)).

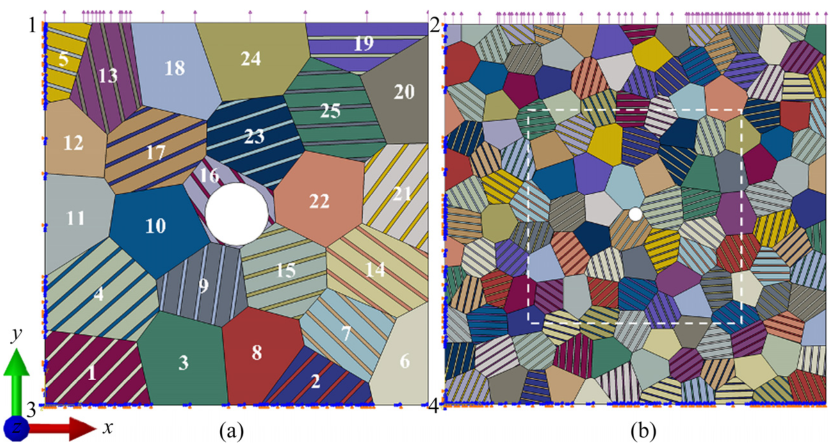

Fig. 2 Fatigue 2D model setup: (a) 25-grain model with microvoid diameter of 10 μm; (b) 150-grain model with microvoid diameter of 5 μm, and white dotted area contains about 100 grains

3 Results and discussion

The microplasticity behavior determines the macroscopic properties of the materials. As we all known that deformation accommodate relationship exists between different phases and different structures in titanium alloys. The volume fraction of primary α phase greatly influences the plasticity of the alloy, and the secondary α phase has a great contribution to the strength of materials. The synthetic structure was subjected to cyclic loading for 100 cycles, and the volume fraction of primary α phase and the thickness of the secondary α and β phases were kept constant. Microvoids with different size or curvature k were introduced, and the changes of CSS in each phase or slip system and distribution of GND in material were obtained in this section.

3.1 Effect of microvoids on GND density

Heterogeneous deformation at the boundary of the material is accommodated by the GND, which essentially reflects the lattice incompatibility. It is reasonable to believe that the generation of fatigue cracks is the result of incompatible lattices and heterogeneous deformation. Consequently, it is appropriate to use the distribution of GND density as an indicator of fatigue performance. The orientation of each grain and the elastic modulus of each phase are both different, which results in different deformation gradients between each part. As shown in Figs. 3(a) and (b), GND is mainly concentrated in the grain and at the phase boundaries, but whose density at the boundaries of the primary α phase grains is very small. However, when the microvoid defects are introduced into the microstructure, a concentrated GND is generated nearby the microvoids, and the density of which is large. After the statistics of each integration point of the model (errors caused by the grid distortion have been removed), the calculation shows that the existence of microvoid defects caused the average GND density in the whole model to increase from 1.78×10^{13} to 2.85×10^{13} m^{-2}. It can be concluded that the existence of microvoids is indicative of an

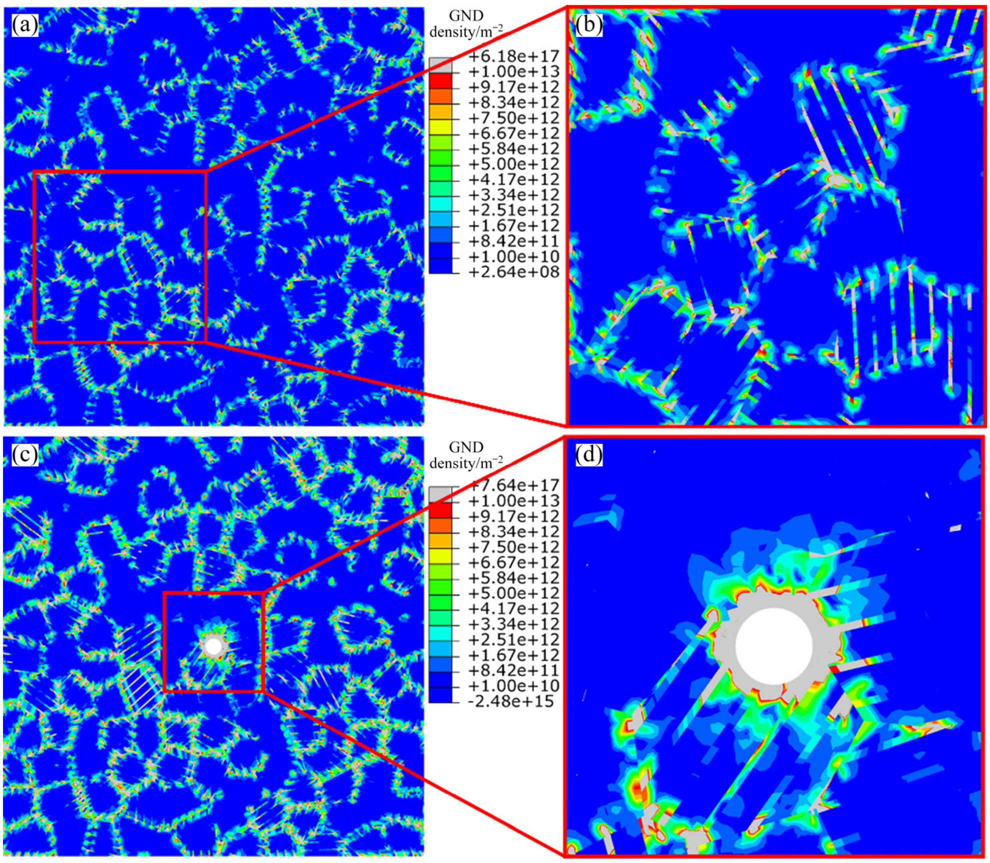

Fig. 3 Distribution maps of GND in non-defective and defective models: (a) Distribution of GND density in 150-grain non-defective model; (b) Partially enlarged part in (a); (c) Distribution of GND density in 150-grain defective model; (d) Partially enlarged part in (c)

increase in the heterogeneity of material deformation.

The effect of the microvoid on the GND density in the microstructure has been studied in detail. In order to weaken the boundary effects on the average GND density, simulations have been carried out on the model with 100 grains. The variation of average GND density with the microvoids parameters is shown in Fig. 4. It can be clearly seen that with the increase of the area of the voids or the TPZ curvature, the average GND density increases. It can also be seen that the influence of TPZ curvature on average GND density is greater than that of the area of the voids. The elongated voids have a great influence on the heterogeneity of local deformation.

3.2 Effect of microvoids on CSS in primary *α*, secondary *α* and *β* phases

After 100 cycles of fatigue simulations on the non-defective and defective models, the distribution maps of CSS are shown in Figs. 5(a) and (b), respectively. It can be clearly seen that large CSS are mainly distributed in the *β* phase and primary *α* phase. The effect of microvoids on the distribution and value of the CSS was studied by a synthetic structure with a TPZ curvature of 7 μm^{-1} of the microvoid. When the microvoid was introduced into the model, the heterogeneity of the deformation of the material increased, and the accommodation of grain deformation near the microvoid became more difficult. Compared with the non-defective model, Fig. 5 shows that CSS distributes with a shape of "butterfly wings" around the microvoid, and the grains closer to the microvoid (Grains $10^{\#}$, $15^{\#}$, $16^{\#}$, $17^{\#}$, and $22^{\#}$) also have a large CSS. The CSS values of each phase in two models are counted, and it can be seen that during the cyclic loading, the CSS in each phase gradually accumulates, and the appearance of microvoids causes the CSS value in each phase to be larger than that in non-defective model (Fig. 6).

Microvoids with the surface curvature from 0.0032 to 15.7216 μm^{-1} and sizes from 19.63 to 89.63 μm^2 were set into the synthetic structure, whilst the distribution and value of CSS in each

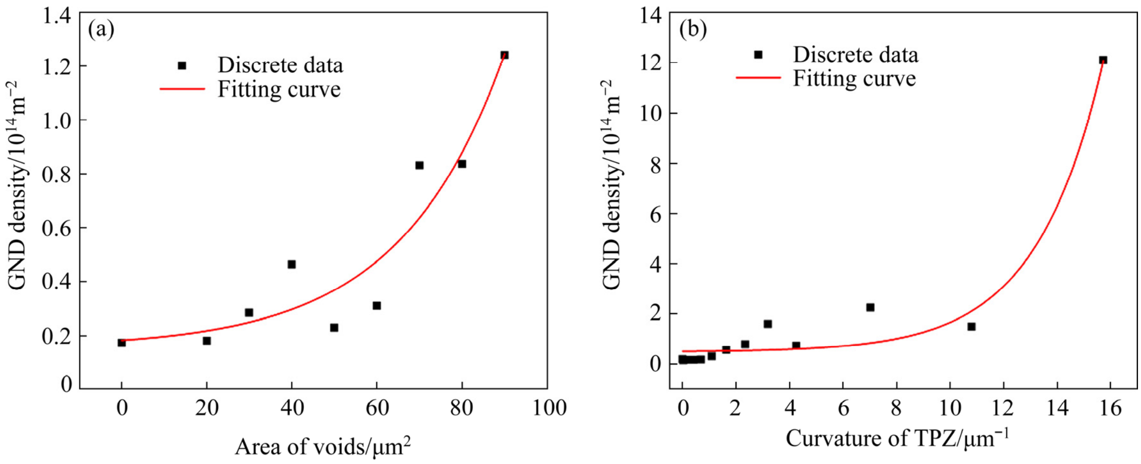

Fig. 4 Variation of average GND density with microvoids parameters: (a) Area of voids; (b) Curvature of TPZ

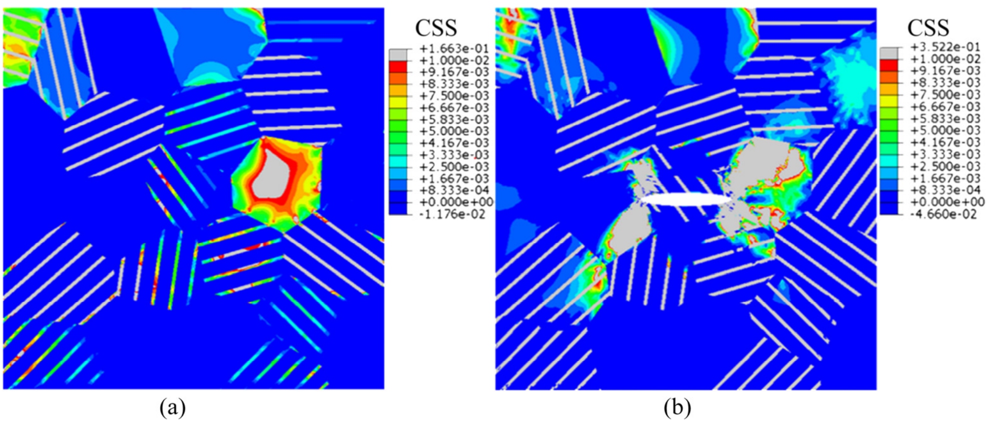

Fig. 5 Distribution maps of CSS in non-defective (a) and defective (b) models

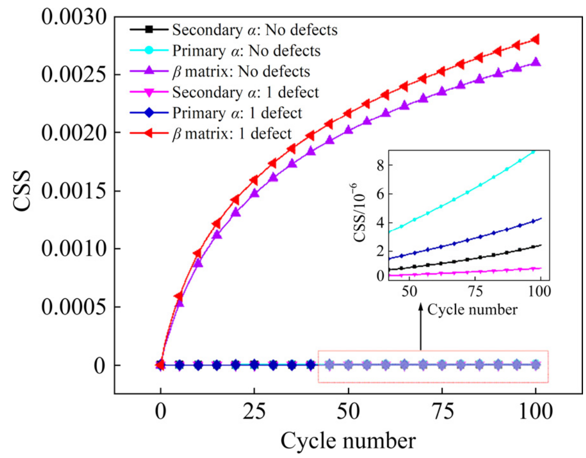

Fig. 6 Curves of CSS of each phase in defective and non-defective models with cyclic loading

phase were calculated. And the degree of deviation ς from each result to the non-defective model was used to indicate the degree of influence of microvoid parameters on the CSS and calculated by the formula:

$$\varsigma=\frac{\varepsilon_{\text{defective}}^{\text{C}}-\varepsilon_{\text{non-defective}}^{\text{C}}}{\varepsilon_{\text{non-defective}}^{\text{C}}} \tag{13}$$

where $\varepsilon_{\text{defective}}^{\text{C}}$ and $\varepsilon_{\text{non-defective}}^{\text{C}}$ are CSS values in defective and non-defective models, respectively.

Figure 7 shows that as the curvature of TPZ and the size of the microvoids increase, the CSS average value of each phase in the material increases. It can also be seen that the CSS is easier to accumulate in the β phase than in the α phase, and in the primary α phase it is larger than that in the secondary α phase. With the increase of the curvature and size of the microvoid, CSS in the secondary α phase grows fastest, and the primary α and β phases have a similar growth rate but the latter was a bit larger. The deformation at the α/β interface between secondary α phase and β phase is difficult to accommodate. Compared with uniform primary α grains, the lamellar structure is more sensitive to stress and strain. Due to the heterogeneous local deformation, the serious concentration of stress and strain is more likely to occur in the lamellar structure. Figure 7 shows that the effect of curvature on CSS is greater than that of the size. When the curvature k continues to increase, the effect is closer to the effect of cracks, and large stress and strain will be generated at its tip, which has a great impact on the initiation and propagation of fatigue cracks.

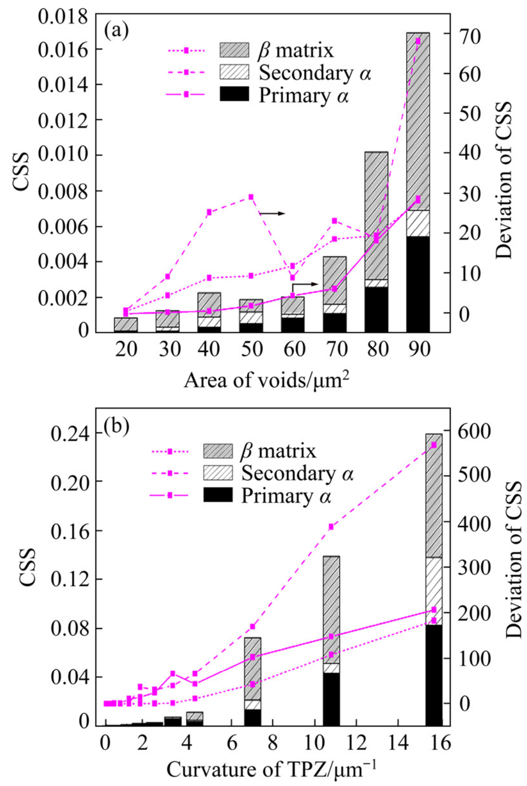

Fig. 7 Influence of area of voids (a) and curvature of TPZ (b) on CSS in different phases (Histogram represents value of CSS, and line graph represents deviation of CSS)

3.3 Effect of microvoids on CSS in different slip systems

Figure 8 shows that a severe strain concentration appears in the adjacent grains of the microvoids when a microvoid is introduced into the synthetic structure, especially in Grains 10# and 22#. The CSS also increases inside Grain 16# due to the shear effect. Because Grain 22# is the softest and Grain 10# is the hardest, the maximum CSS at the Grain 10#/16# boundary appears on Grain 16# side, and the CSS maximum at the Grain 16#/22# boundary is distributed on Grain 22# side (Fig. 8). The deviation degree ς of the CSS values in the three grains was calculated. As shown in Fig. 9, the microvoid causes the CSS value in each slip system to increase. Grains 10# and 22# suffer severely concentrated shear stress, and the CSS value on the prismatic slip system changes a lot, while CSS value on the basal slip system in Grain 16# with principal stress concentration changes greatly. Consequently, in addition to being sensitive to crystal orientation, the slip system is also sensitive to the stress state.

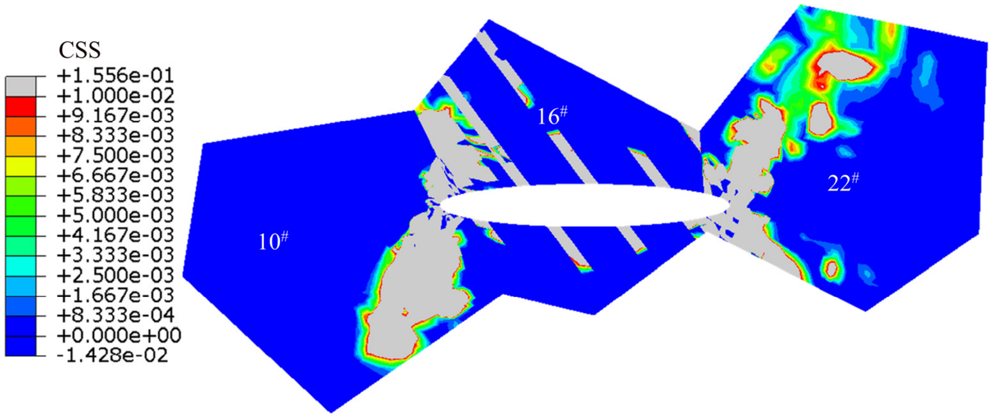

Fig. 8 Distribution of CSS in Grains 10#, 16# and 22#

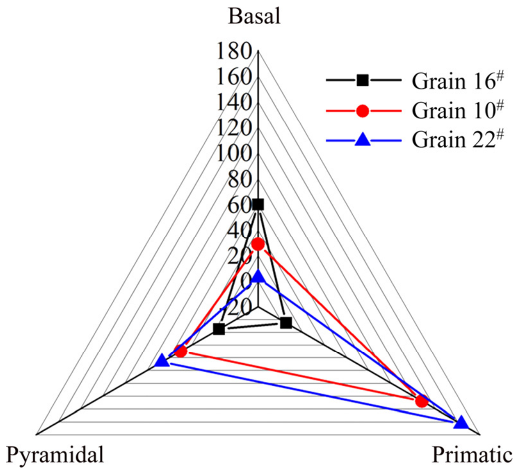

Fig. 9 Deviation of CSS of Grains 10#, 16# and 22#

With the increase of curvature and size of the microvoid, the resistance of deformation increases, and the heterogeneity of material deformation increases. The CSS values in the slip system in a model containing a microvoid with different curvature or size were calculated out. As shown in Fig. 10, as the curvature and size of the microvoid increase, the CSS magnitude in each group of slip system in the material increases, which is mainly concentrated in the prismatic slip system. The degree of deviation of the CSS in all α-phase slip systems about the microvoids characteristic was calculated. The results show that the microvoid has great influence on the average CSS value in the prismatic slip system.

In this work, a double-microvoids model has been established to study the effect of aggregation degree of microvoids on the deformation behavior, in which the two microvoids are with a size of 5 μm and curvature of 0.4 μm^{-1} (Fig. 11(a)). And the distance L between two microvoids changes in the

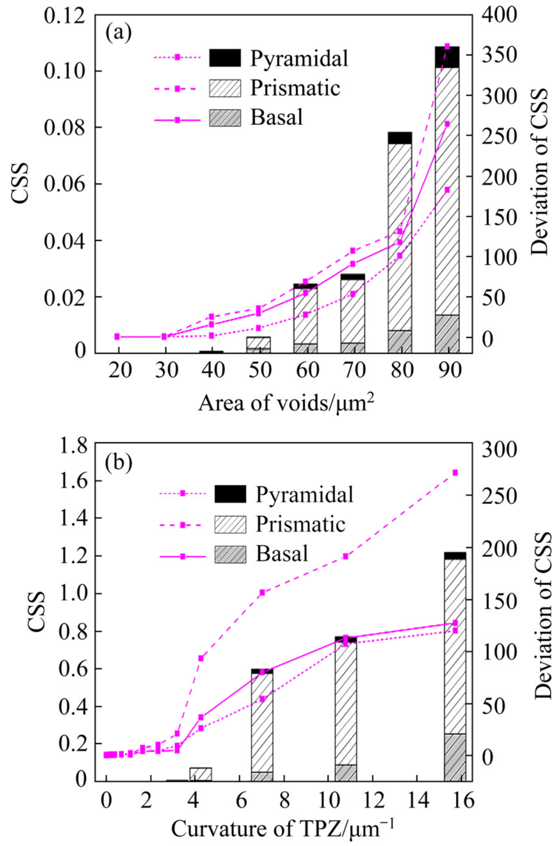

Fig. 10 Influence of area of voids (a) and curvature of TPZ (b) on CSS in each slip systems (Histogram represents value of CSS, and line graph represents deviation of CSS)

range of 6−14 μm. The accumulation of microvoids results in a thin bridge region in the material, which is subjected to strong shearing effects (Fig. 11(b)). The CSS distribution maps of the double-microvoids model with different L values are shown in Fig. 12. It can be clearly seen that when L is equal to 6 μm, a severe strain accumulation will appear in the thin bridge region (Fig. 12(a)), which

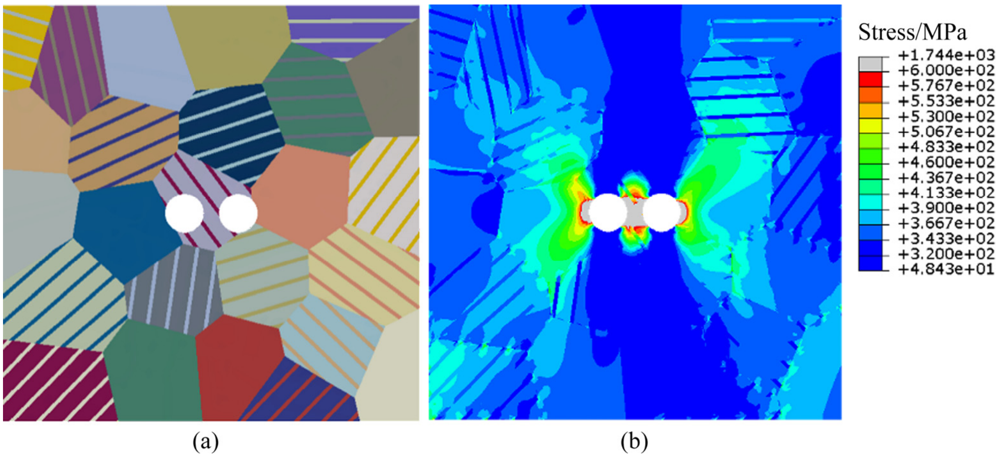

Fig. 11 Schematic diagram (a) and stress distribution (b) in double-microvoids model

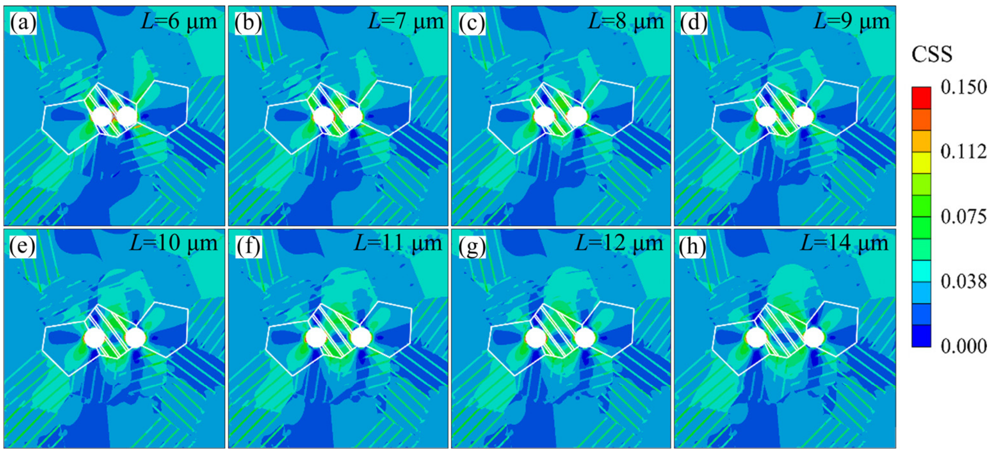

Fig. 12 Distribution of CSS in double-microvoids model with different *L* values

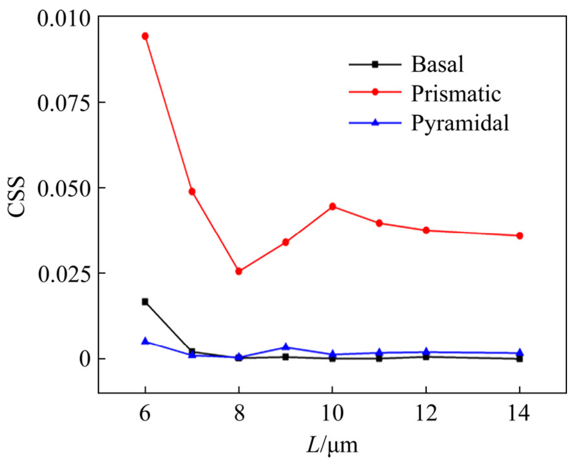

Fig. 13 Dependence of CSS on distance *L*

is because the large shear effect promotes the activation of the slip system. The variation of the average value of CSS in each slip system in the thin bridge region with L is shown in Fig. 13. With the increase of the distance L, CSS in each slip system decreases firstly, and when L reaches 8 μm, the CSS value increases slightly and then gets a constant level, which is because as L increases, the double microvoids gradually enter the primary α phase (Grains $10^{\#}$ and $22^{\#}$), resulting in an increase in the overall average CSS. When L continues to increase, the local CSS accumulation phenomenon caused by the severe shear effect in the thin bridge region gradually weakens. Hence, the multi-microvoids greatly affect the strain uniformity in the microstructure and cause a serious strain accumulation in the prismatic slip system in the weak area such as the thin bridge region, which often results in crack initiation and propagation during fatigue loading.

4 Conclusions

(1) The GND tends to cumulate around the microvoids. The influence of curvature in the TPZ on GND density is greater than that of the area of the void.

(2) With the increase of the microvoid size or the curvature of TPZ, CSS in primary α, secondary α and β phases increases. The CSS in the secondary α phase is greatly influenced by the size or curvature of the microvoid.

(3) The CSS in each slip system of the primary α phase increases with the increase of the size and curvature of the microvoid, and the CSS of the prismatic slip system is dominant in the primary α phase.

(4) The CSS greatly accumulates between the voids. As the distance L between the two microvoids gradually increases, the CSS value in each slip system gradually decreases so that the interactive effects of the microvoids are weaken. When the distance L is larger than 8 μm, the CSS value in each slip system gets a constant level.

Acknowledgments

This work was financially supported by the National Key Research and Development Program of China (No. 2021YFB3702603).

References

[1] LEYENS C, PETERS M. Titanium and titanium alloys: Fundamentals and applications [M]. Weinheim: Wiley-VCH, 2003.

[2] CUI Shu-wan, SHI Yong-hua, ZHANG Cheng-shi. Microstructure and mechanical properties of TC4 titanium alloy K-TIG welded joints [J]. Transactions of Nonferrous Metals Society of China, 2021, 31(2): 416−425.

[3] ZHOU Li, YU Ming-run, CHEN Wei-guang, ZHANG Zi-li, DU Shuai, LIU Hui-jie, YU Yan, GAO Fu-yang. Microstructure and mechanical properties of friction stir processed TA5 alloy [J]. Transactions of Nonferrous Metals Society of China, 2021, 31(2): 404−415.

[4] ASIM U B, SIDDIQ M A, KARTAL M E. A CPFEM based study to understand the void growth in high strength dual-phase titanium alloy (Ti−10V−2Fe−3Al) [J]. International Journal of Plasticity, 2019, 122: 188−211.

[5] OBERWINKLER B, RIEDLER M, EICHLSEDER W. Importance of local microstructure for damage tolerant light weight design of Ti−6Al−4V forgings [J]. International Journal of Fatigue, 2010, 32: 808−814.

[6] ERMATCHENKO A G, KASHAEV R M. Production of aircraft engine compressor rotor discs with desired service life in titanium alloys [J]. Materials Physics & Mechanics, 2011, 11: 118−125.

[7] LIU Yun-xi, CHEN Wei, LI Zhi-qiang, TANG Bin, HAN Xiu-quan, YAO Gang. The HCF behavior and life variability of a Ti−6Al−4V alloy with transverse texture [J]. International Journal of Fatigue, 2017, 97: 79−87.

[8] LIANG Xiao-yu, ROBERT C, HOR A, MOREL F. A numerical investigation of the high cycle fatigue sensitivity to microstructure and defect [J]. International Journal of Fatigue, 2020, 136: 105541.

[9] YANG Kun, ZHONG Bin, HUANG Qi, HE Chao, HUANG Zhi-yong, WANG Qing-yuan, LIU Yong-jie. Stress ratio effect on notched fatigue behavior of a Ti−8Al−1Mo−1V alloy in the very high cycle fatigue regime [J]. International Journal of Fatigue, 2018, 116: 80−89.

[10] MURUGAN G, RAGHUKANDAN K, PILLAI U T S, PAI B C. Modeling of the effect of a defect on HCF life of a magnesium AZ91 specimen subjected to transverse load [J]. Procedia Engineering, 2013, 55: 768−773.

[11] FOMIN F, KASHAEV N. Influence of porosity on the high cycle fatigue behaviour of laser beam welded Ti−6Al−4V butt joints [J]. Procedia Structural Integrity, 2017, 7: 415−422.

[12] FOMIN F, HORSTMANN M, HUBER N, KASHAEV N. Probabilistic fatigue-life assessment model for laser-welded Ti−6Al−4V butt joints in the high-cycle fatigue regime [J]. International Journal of Fatigue, 2018, 116: 22−35.

[13] VANSICKLE R, FOEHRING D, SHEW H B, LAMBROS J. Microstructure effects on fatigue crack growth in additively manufactured Ti−6Al−4V [J]. Materials Science and Engineering A, 2020, 795: 139993.

[14] MAENOSONO A, KOYAMA M, TANAKA Y, RI S, WANG Qing-hua, NOGUCHI H. Crystallographic selection rule for the propagation mode of microstructurally small fatigue crack in a laminated Ti−6Al−4V alloy: Roles of basal and pyramidal slips [J]. International Journal of Fatigue, 2019, 128: 105200.

[15] TANAKA K, MURA T. Fatigue crack growth along planar slip bands [J]. Acta Metallurgica, 1984, 32: 1731−1740.

[16] LI Zi-han, ZHOU Guo-wei, LI Da-yong, WANG Hua-miao, TANG Wei-qin, PENG Ying-hong, ZUROB H S, WU Pei-dong. Crystal plasticity based modeling of grain boundary sliding in magnesium alloy AZ31B sheet [J]. Transactions of Nonferrous Metals Society of China, 2021, 31(1): 138−155.

[17] HU Li, JIANG Shu-yong, SHI Lai-xin, ZHANG Yan-qiu. Prediction of grain scale plasticity of NiTi shape memory alloy based on crystal plasticity finite element method [J]. Transactions of Nonferrous Metals Society of China, 2019, 29(4): 775−784.

[18] TURKMEN H S, LOGE R E, DAWSON P R, MILLER M P. On the mechanical behaviour of AA 7075-T6 during cyclic loading [J]. International Journal of Fatigue, 2003, 25: 267−281.

[19] SINHA S, GHOSH S. Modeling cyclic ratcheting based fatigue life of HSLA steels using crystal plasticity FEM simulations and experiments [J]. International Journal of Fatigue, 2006, 28: 1690−1704.

[20] GHOSH S, CHAKRABORTY P. Microstructure and load sensitive fatigue crack nucleation in Ti-6242 using accelerated crystal plasticity FEM simulations [J]. International Journal of Fatigue, 2013, 48: 231−246.

[21] LU Xu, DUNNE F P E, XU Yi-lun. A crystal plasticity investigation of slip system interaction, GND density and stored energy in non-proportional fatigue in nickel-based superalloy [J]. International Journal of Fatigue, 2020, 139: 105782.

[22] PRASTITI N G, XU Yi-lun, BALINT D S, DUNNE F P E. Discrete dislocation, crystal plasticity and experimental studies of fatigue crack nucleation in single-crystal nickel [J].

International Journal of Plasticity, 2020, 126: 102615.
[23] BRIFFOD F, SHIRAIWA T, ENOKI M. Microstructure modeling and crystal plasticity simulations for the evaluation of fatigue crack initiation in α-iron specimen including an elliptic defect [J]. Materials Science and Engineering A, 2019, 695: 165−177.
[24] MORRISSEY R J, MCDOWELL D L, NICHOLAS T. Microplasticity in HCF of Ti−6Al−4V [J]. International Journal of Fatigue, 2001, 23: 55−64.
[25] HUTCHINSON J W, GANTEN D, SCHELLING P, YLITALO P, MOHRING J, KALINA M. Bounds and self-consistent estimates for creep of polycrystalline materials [J]. Proceedings of the Royal Society of London (Series A): Mathematical and Physical Sciences, 1976, 348: 101−127.
[26] CHABOCHE J L. Constitutive equations for cyclic plasticity and cyclic viscoplasticity [J]. International Journal of Plasticity, 1989, 5: 247−302.
[27] YAGUCHI M, TAKAHASHI Y. Ratchetting of viscoplastic material with cyclic softening. Part 2: Application of constitutive models [J]. International Journal of Plasticity, 2005, 21: 835−860.
[28] ANAHID M, SAMAL M K, GHOSH S. Dwell fatigue crack nucleation model based on crystal plasticity finite element simulations of polycrystalline titanium alloys [J]. Journal of the Mechanics and Physics of Solids, 2011, 59: 2157−2176.
[29] ASARO R J, NEEDLEMAN A. Texture development and strain-hardening in rate dependent polycrystals [J]. Acta Metallurgica, 1985, 33: 923−953.
[30] PEIRCE D, ASARO R J, NEEDLEMAN A. Material rate dependence and localized deformation in crystalline solids [J]. Acta Metallurgica, 1983, 31: 1951−1976.
[31] ASHBY M F. The deformation of plastically non-homogeneous materials [J]. Journal of Theoretical Experimental and Applied Physics, 1970, 21: 399−424.
[32] ACHARYA A, BEAUDOIN A J. Grain-size effect in viscoplastic polycrystals at moderate strains [J]. Journal of the Mechanics and Physics of Solids, 2000, 48: 2213−2230.
[33] HAN Feng-bo, TANG Bin, YAN Xu, PENG Yi-fei, KOU Hong-chao, LI Jin-shan, DENG Ying, FENG Yong. Indentation pileup behavior of Ti−6Al−4V alloy: Experiments and nonlocal crystal plasticity finite element simulations [J]. Metallurgical and Materials Transactions A, 2017, 48: 2051−2061.
[34] ZHANG M Q, TANG B, YANG R M, WILLIAM W Y, KOU H C, LI J S. Combined crystal plasticity simulations and experiments for parameter identification: Application to near-β titanium alloy [J]. Journal of Materials Science, 2020, 55: 15043−15055.
[35] NYE J F. Some geometrical relations in dislocated crystals [J]. Acta Metallurgica, 1953, 1: 153−162.
[36] BRIDIER F, MCDOWELL D L, VILLECHAISE P, MENDEZ J. Crystal plasticity modeling of slip activity in Ti−6Al−4V under high cycle fatigue loading [J]. International Journal of Plasticity, 2009, 25(6): 1066−1082.
[37] BATTAILE C C, EMERY J M, BREWER J N, BOYCE B L. Crystal plasticity simulations of microstructure-induced uncertainty in strain concentration near voids in brass [J]. Philosophical Magazine, 2015, 95: 1069−1079.

微孔洞对高周循环载荷作用下双相钛合金微塑性行为的影响(I)：晶体塑性分析

李凯迪 [1]，韩晓宁 [2]，唐 斌 [1]，张梦琪 [1]，李金山 [1]

1. 西北工业大学 凝固技术国家重点实验室，西安 710072；
2. 北京航空制造技术研究院，北京 100024

摘 要：建立二维晶体塑性有限元模型研究微孔洞与高周循环载荷作用下双相钛合金微塑性变形行为的关系。结果表明，几何必需位错(GND)倾向聚集于微孔洞周围，且导致平均 GND 密度升高。孔洞尖端塑性区域（TPZ）的曲率对 GND 密度的影响大于孔洞尺寸的影响。随着 TPZ 曲率和空洞尺寸的增大，初生 α、次生 α 及 β 基体内的累积剪切应变增大。初生 α 相内柱面滑移系上的累积剪切应变主导其变形。当微孔洞间距增大时，微孔洞对累积剪切应变的影响减弱。

关键词：晶体塑性；双相钛合金；微孔洞；高周循环载荷；累积剪切应变；几何必需位错

(Edited by Wei-ping CHEN)